$^{14}N + {}^{10}B$ Fusion and Elastic Scattering Cross Section Measurements near the Interaction Barrier[†]

Shiu-Chin Wu, J. C. Overley[††] and C. A. Barnes

W. K. Kellogg Radiation Laboratory

California Institute of Technology, Pasadena, California 91125, U.S.A.

and

Z. E. Switkowski[‡]

School of Physics

University of Melbourne, Parkville 3052, Australia[‡‡]

and

W. K. Kellogg Radiation Laboratory

California Institute of Technology, Pasadena, California 91125, U.S.A.

[†]Supported in part by the National Science Foundation [PHY76-83685].

[††]Permanent address: Physics Department, University of Oregon, Eugene, Oregon 97403.

[‡]Queen Elizabeth II Fellow.

[‡‡]Present address.

Abstract — The $^{14}N + ^{10}B$ fusion reactions were studied at c.m. energies between 2.9 and 7.5 MeV by measuring the yields of γ-rays from the residual nuclei formed by particle evaporation from the compound system. Cross sections for formation of the evaporation residues ^{16}O, ^{19}F, ^{19}Ne, ^{20}Ne, ^{21}Ne, ^{22}Ne, ^{22}Na, ^{23}Na and ^{23}Mg, as well as the total cross section, were deduced from these yields with the aid of statistical model calculations. $^{14}N + ^{10}B$ elastic scattering differential cross sections were measured from $E_{c.m.} = 4.3$ to 9.1 MeV at $\theta_{c.m.} = 74.4^{o}$, and from $E_{c.m.} = 3.3$ to 8.3 MeV at $\theta_{c.m.} = 90.0^{o}$. The elastic scattering cross sections were analyzed within the framework of the incoming-wave boundary condition (IWBC) model. The fusion cross sections calculated for the real ion-ion potential deduced from the IWBC model fit to the elastic scattering are in good agreement with the measured values.

Key Words

NUCLEAR REACTIONS $^{10}B(^{14}N,X)$, $E_{c.m.}$ = 2.9-7.5 MeV; measured σ, γ-ray yields from ^{16}O, ^{19}F, $^{19,20,21,22}Ne$, $^{22,23}Na$, ^{23}Mg; deduced total fusion σ. $^{10}B(^{14}N,^{14}N)$, $E_{c.m.}$ = 4.3-9.1 MeV measured $\sigma(74.4^{\circ})$, $E_{c.m.}$ = 3.3-8.3 MeV measured $\sigma(90.0^{\circ})$. Enriched target. IWBC analysis.

1. Introduction

Certain heavy-ion fusion reactions, particularly those involving ^{12}C and ^{16}O, are of great importance for element synthesis during the later evolutionary stages of stars[1]. Reaction rates for these processes have usually been predicted by extrapolating measured cross sections downward to energies of astrophysical interest after first extracting the strong energy dependence expected from s-wave Coulomb-barrier penetration[2]. Uncertainties in the extrapolations have sparked interest in the low-energy systematics of fusion reactions in general, and several examples have now been studied[3]. More recently, studies of fusion processes have been coupled with elastic scattering measurements. Optical model or incoming-wave boundary condition (IWBC) parameters are deduced from the data, and the models are then used as guides in the extrapolation of fusion cross sections to lower energies[4,5].

Although most measured fusion reaction cross sections have a smooth energy dependence below the Coulomb barrier, the $^{12}C + ^{12}C$ and $^{12}C + ^{16}O$ fusion cross sections fluctuate with energy[6-9]. Hypotheses adduced to explain this behavior include: compound nucleus fluctuations arising from overlapping resonances, "quasi-molecular" resonances or some other form of intermediate structure, and entrance-channel effects dependent on the microscopic structure of the interacting nuclei[10].

The $^{14}N + ^{10}B$ reaction is of special interest in this regard, for it forms the same compound system as the $^{12}C + ^{12}C$ reaction. Figure 1 illustrates the Q-values for formation of the compound nucleus, ^{24}Mg, and indicates most of the residual nuclei which can be formed by subsequent particle evaporation. Because the $^{14}N + ^{10}B$ reaction forms ^{24}Mg at much higher excitation energies

than the $^{12}C + ^{12}C$ reaction, compound nucleus resonance fluctuation effects should be considerably reduced by the higher level density. Furthermore, the microscopic structures of the two pairs of interacting nuclei are very different, with α-particle clustering presumably of less importance in the $^{14}N + ^{10}B$ case. Although these features of the $^{14}N + ^{10}B$ system would lead one to expect no structure in the energy dependence of the reaction cross section[10,11], structure has been observed in the $^{10}B(^{14}N,\alpha)^{20}Ne$ reaction at energies above the Coulomb barrier[12].

Two quite different experimental techniques have been reported for the measurement of fusion cross sections by observing the deexcitation γ-rays from the residual nuclei. The first[5,8] employs two large high-efficiency NaI scintillators, each subtending a solid angle of nearly 2π sr at the target. The spectra of non-coincident events are summed and total fusion cross sections are deduced after correcting for background, non-radiative transitions, and detection efficiency. The second technique[13] employs a single high-resolution Ge(Li) detector to identify the formation of particular residual nuclei by observing transitions between low-lying states populated mainly through deexcitation cascades. This technique has the advantage that the cross sections for production of different residual nuclei can be determined, as well as the total fusion cross section.

We have used the latter technique to determine $^{14}N + ^{10}B$ fusion reaction cross sections between $E_{c.m.} = 2.9$ and 7.5 MeV. During the course of the present measurements, High and Čujec[14] reported a similar measurement which employed the former technique. Their data are compared with the results of the present investigation in the concluding section of the paper.

In addition to studying the $^{14}N + ^{10}B$ fusion cross sections, we have also measured $^{14}N + ^{10}B$ elastic scattering excitation functions at laboratory

angles $\theta_{lab} = 30.0^{\circ}$ and 35.5°, corresponding to $\theta_{c.m.} = 74.4^{\circ}$ and 90.0°, respectively. The scattering data have been used to determine the parameters of the real ion-ion potential within the framework of the IWBC model[4]. The IWBC model has then been used to calculate expected fusion cross sections for comparison with the measured cross sections.

2. Experimental Methods

2.1 TARGETS

Targets were prepared by electron-beam evaporation of elemental boron isotopically enriched to 96.2% ^{10}B. For the γ-ray yield measurements, the boron was deposited on spectroscopically pure copper discs 0.25 mm thick. Thin transmission targets were used for the elastic scattering measurements. For the targets employed in the scattering measurements at $\theta_{c.m.} = 74.4^{\circ}$, boron was evaporated onto a $BaCl_2$-coated glass substrate. A gold layer approximately $2\,\mu g/cm^2$ thick was flashed over the boron and the composite foils were floated in water from the substrate onto the target holders. For the targets used at $\theta_{c.m.} = 90^{\circ}$, the boron and gold layers were deposited on a glass substrate previously coated with a $5\,\mu g/cm^2$ carbon film. Films of the latter type, similarly floated onto target holders, were considerably sturdier than those without the carbon films. The thicknesses of the boron layers were monitored continuously during the boron evaporation, and were limited to values between 5 and 15 $\mu g/cm^2$.

The elemental compositions of the transmission targets were investigated by α-particle elastic scattering measurements at $E_{lab} = 1.5$ MeV and $\theta_{lab} = 60^{\circ}$. Scattered α-peaks from ^{10}B, ^{11}B, ^{12}C, ^{16}O and ^{197}Au were clearly resolved. The energy and angle dependence of the elastic scattering yields were checked

and found to be consistent with pure Coulomb scattering. Rutherford scattering cross sections were therefore used to deduce target compositions. Because of possible uncertainties in the ^{4}He beam current integration, the boron and gold contents of the targets were verified in a proton elastic scattering experiment at 2.2 MeV and $\theta_{lab} = 120^{\circ}$. Previously measured[15] $^{10}B(p,p)^{10}B$ cross sections were used to deduce the ^{10}B content, and the Rutherford cross section was used to deduce the gold content. The target compositions derived from both α-particle and proton scattering were consistent within ± 10%. A typical carbon-backed target contained 12.8 $\mu g/cm^2$ of ^{10}B, 8.0 $\mu g/cm^2$ of ^{12}C, 3.3 $\mu g/cm^2$ of ^{16}O and 2.3 $\mu g/cm^2$ of ^{197}Au.

The ^{10}B content of the copper-backed targets was also determined by proton elastic scattering at $E_{lab} = 2.183$ MeV and $\theta_{lab} = 140^{\circ}$. At this energy and angle the elastic scattering cross section passes through a broad maximum and $\sigma/\sigma(Ruth) = 9.9$ (ref.[15]). Thus, although the ^{10}B scattering peak was superimposed on the thick-target scattering yield from the copper substrate, as shown in fig. 2, the ^{10}B scattering yield could be determined to ± 2% in a short time.

Copper-backed targets for which the ^{10}B content had been determined by elastic proton scattering were also bombarded by ^{14}N and ^{16}O ions, and the yields of the 718 keV γ-rays arising from Coulomb excitation of the first excited state of ^{10}B were measured. Heavy ion Coulomb excitation studies of ^{10}B have been reported previously by Andreev et al.[16]. Coulomb excitation cross sections were calculated with a $B(E2\uparrow)$ value of 1.80 e^2 fm^4, deduced from the reported lifetime of 1.013 ± 0.015 nsec for the first excited state[17]. Since the Coulomb excitation cross sections are calculated to be isotropic to within 2%, it is straightforward to deduce the ^{10}B content of the target if Coulomb excitation is the dominant source of 718 keV γ-rays.

Fig. 3

Figure 3 shows the calculated Coulomb excitation cross sections for both ^{14}N and ^{16}O projectiles. Also shown are the measured γ-ray yields normalized to the calculations. The ^{10}B content of the target deduced from this normalization factor and the measured γ-ray detection efficiency agrees within ± 5% with that deduced from the proton elastic scattering measurements. The agreement between the two methods of determining the ^{10}B content of the copper-backed targets is very useful, as all γ-ray spectra acquired during the fusion studies include well-resolved peaks at 718 keV, which then provide a built-in monitor of the ^{10}B target content. The Coulomb excitation technique was also used to determine the amount of ^{10}B in the targets used in the fusion cross section measurements. For the targets used in the present study, these amounts ranged from 6 to 10 $\mu g/cm^2$.

Čujec and Barnes[8]) have pointed out that it is also important to know the total energy-loss in targets used in fusion studies since fusion cross sections vary rapidly with energy below the barrier. The energy-loss thicknesses of targets used in the present studies were deduced by profiling[18]) the hydrogen contamination in the evaporated layers with the $^{1}H(^{19}F,\alpha\gamma)^{16}O$ reaction. Resonances corresponding to ^{19}F beam energies of

Fig. 4

both 6.40 and 16.44 MeV[19]) were used. Figure 4 shows examples of the profiles obtained at the two resonances. The widths (in energy units) of the hydrogen distributions, measured as the interval between the half-maximum points at the leading and trailing edges, were corrected for the natural resonance widths to obtain the energy-loss thicknesses for ^{19}F ions. These were converted to thicknesses for other ions with the stopping-power tables of Northcliffe and Schilling[20]). The energy-loss thicknesses of the targets were greater than expected from the measured ^{10}B content alone because of contributions to the energy loss from impurities. The amounts of ^{12}C and

^{16}O contaminations required to increase the energy-loss thickness to the observed values were consistent with the ^{12}C and ^{16}O quantities found to be present in the self-supporting targets where the ^{12}C and ^{16}O could be measured directly. A quantitative measure of the ^{12}C and ^{16}O impurities in the thick-backed targets was obtained during the fusion cross section measurements to be described later. The hydrogen distributions shown in fig. 4 indicate some inhomogeneity of target composition. The targets were sufficiently thin, however, that inhomogeneity effects could be ignored in determining the effective beam energy in the ^{10}B target.

2.2 FUSION CROSS SECTION MEASUREMENTS

Momentum-analyzed beams of ^{14}N ions in the 3^+ and 4^+ charge states were delivered by the ONR-CIT tandem Van de Graaff accelerator. Targets were oriented perpendicular to the beam, in a deep Faraday cup maintained at an ambient pressure $\leq 2 \times 10^{-8}$ Torr. Secondary electrons were suppressed electrostatically, and beam currents were integrated conventionally with an accuracy estimated as better than ± 5%. Beam currents ranged from 750 nA at the lowest energies to 25 nA at the highest. Beam currents were limited to keep the detection electronics dead times below 12%. Integrated beam charge ranged from 5 mC to 18 μC per point as required.

A 73 cm^3 coaxial Ge(Li) detector was centered at 0^o with respect to the beam and was shielded circumferentially by a minimum of 10 cm of lead. The detector was placed as close to the target as feasible, usually with the Germanium crystal surface about . cm from the target. For one run, 3 mm of lead shielding was inserted between the detector and the target, but for the remainder of the work the lead was removed to improve the detection efficiency of low-energy γ-rays.

This experimental arrangement, which has been described in more detail elsewhere[9], was used both for the fusion studies and for the studies of the usefulness of Coulomb excitation for target analysis. The measurements of the energy-loss thicknesses of the targets were made with the same target chamber, but with the Ge(Li) detector replaced by an unshielded 12.7 cm diameter by 10.2 cm thick NaI(Tl) scintillator.

The Ge(Li) detector photopeak detection efficiencies for γ-rays with energies between 0.12 and 3.3 MeV were determined by placing calibrated sources at the target position for each geometry used. The efficiency was extended to 10.76 MeV by measuring γ-ray yields from the $^{27}Al(p,\gamma)^{28}Si$ resonance at E_p = 992 keV and using the known[21] intensities of γ-rays in the deexcitation cascade relative to the 1.779 MeV transition. These efficiencies are measured to an accuracy of ± 5%. The total efficiencies required for summing corrections were calculated for each geometrical configuration.

The γ-ray yield data were accumulated as 4096-channel pulse height spectra. These were obtained at 0.2 MeV intervals for ^{14}N beam energies between 7.8 and 18.0 MeV. Data were also obtained at 7.0 and 7.5 MeV, but with poor counting statistics. Analyzer dead-time corrections were made by a live-charge beam integration technique. Occasional "beam-off" backgrounds were measured to insure that build-up of delayed activities was not significant.

An example of a γ-ray pulse height spectrum is shown in fig. 5 with the numbered full-energy peaks identified in table 1. Gamma rays were observed from residual nuclei formed by single-particle evaporation from the compound system (^{20}Ne, ^{23}Na, ^{23}Mg) and by two-particle evaporation (^{16}O, ^{19}F, ^{19}Ne, ^{22}Ne and ^{22}Na). Although several three-particle evaporation channels are open, with the exception of ^{21}Ne no residual nucleus formed by this process

was observed. A complete data set was obtained with the gain illustrated in fig. 5. A second complete set was obtained at lower gain to include the 6.131 MeV γ-rays from ^{16}O.

As indicated in table 1, lines from ^{22}Na and ^{21}Ne can also be generated by ^{14}N fusion with ^{12}C target impurities. Fusion of ^{16}O or ^{12}C nuclei with ^{14}N may also produce the 585 keV line from the ^{25}Mg first excited state. At high ^{14}N beam energies, more lines than those displayed in fig. 5 were observed. These include lines at 1779 keV, attributed to ^{28}Si formed through ^{14}N fusion with ^{16}O, and at 390 keV from ^{25}Mg which is formed through fusion of ^{14}N with both ^{16}O and ^{12}C. The intensities of these lines and previously measured cross sections[22] were used to estimate the amount of ^{16}O and ^{12}C impurities in the target. The ^{12}C target content obtained this way was consistent with that obtained by assuming that the 1369 keV γ-ray intensity measured at high beam energies was entirely due to ^{24}Mg formed following $^{14}N + ^{12}C$ fusion. It also agreed within ± 10% with the amounts of carbon in the self-supporting foil targets deduced from elastic scattering measurements.

2.3 SCATTERING MEASUREMENTS

All scattering measurements were made in a 61-cm diameter scattering chamber with the incident beam collimated at the entrance to the chamber. An additional collimator directly before the target eliminated beam scattered from the upstream collimator, and limited the position of the beam at the target. Beam current transmitted by the thin targets was collected in a magnetically suppressed Faraday cup. Beam incident on the copper-backed targets was integrated directly on the targets with secondary electrons electrostatically suppressed.

Silicon surface barrier detectors were used to detect the scattered particles. A circular collimator subtending an angle of 2.1° in the θ-direction was used during the target analysis measurements, and detector solid angles were measured with a precision of 4%. Narrower rectangular apertures oriented to have a small subtended angle in the θ-direction were used in the heavy-ion elastic scattering measurements. Angular positioning of the detectors was checked by the positions of the Mott-scattering minima and maximum in the yield of ^{16}O ions scattered near $\theta_{c.m.} = 90°$ from the ^{16}O target contaminations, and was known to within ±0.1°.

An example of a detector pulse-height spectrum, obtained with a 16.4 MeV ^{14}N beam incident on a carbon-film-backed boron target, is shown in fig. 6.

Fig. 6

The yields of ^{14}N ions scattered from ^{10}B were measured relative to those scattered from the gold layer to avoid any possibility of energy-dependent beam current integration errors. Scattering data were taken at $\theta_{lab} = 30°$ at 0.2 MeV intervals from 10.5 to 22 MeV and at $\theta_{lab} = 35.5°$ from 8.0 to 20.0 MeV. In the c.m. system these angles correspond to 74.4° and 90.0°, respectively, and the center of mass energies range from 4 to 9 MeV.

3. Data Reduction

3.1 FUSION CROSS SECTIONS

Cross sections for the formation of the various evaporation residues were determined from spectra similar to that shown in fig. 5. For isotropic γ-ray emission, the relation between the photopeak yield and the cross section is

$$\sigma = \frac{Y}{N\, n\, \Delta x\, \epsilon \beta} \quad , \qquad (1)$$

where N is the number of incident ions, $(n \Delta x)$ is the areal number density of ^{10}B target atoms, and ϵ is the photopeak detection efficiency. The summing-branching factor β is the joint probability that a particular γ-ray is emitted after the residual nucleus is formed and that no other member of a deexcitation cascade is detected in coincidence in the detector[13].

The yield Y in eq. (1) was obtained by summing counts in the photopeak for each γ-ray. Backgrounds were assumed to vary linearly with channel number under the photopeak. The yields of γ-rays from ^{22}Na and ^{21}Ne were corrected for contributions arising from the fusion reactions of ^{14}N with ^{12}C and ^{16}O. These contributions were calculated from the measured ^{12}C and ^{16}O content of the targets, and the measured $^{14}N + ^{12}C$ and $^{14}N + ^{16}O$ fusion cross sections of Switkowski et al.[22]. The gamma rays used in the cross section calculations are indicated in table 1. In those cases where more than one γ-ray is assigned to the same residual nucleus, cross sections were calculated from the intensities of each of the gamma rays and the results were averaged. Similarly, results from runs with different geometries and targets were averaged. The data from different runs were consistent to within ± 8%, while the cross sections deduced from the intensities of different γ-rays from the same nucleus were consistent to within ± 10%.

Cross sections were ascribed to a ^{14}N energy equal to the incident energy minus one-half the energy loss in the boron layer, as deduced from the ^{19}F profiling results. The targets were assumed to be uniform and homogeneous in composition, and no further corrections were made for the non-linear energy dependence of the cross sections. For the thin targets used in the present experiment, these corrections were negligible compared with the effects of the 0.1% uncertainty in the incident beam energy.

The summing and branching factors β were calculated from relative

populations of final states, tabulated[17,23] branching ratios, and calculated total detection efficiencies. When the compound nucleus is formed at sufficiently high excitation energy, the population of a low-lying state of spin J in an evaporation residue should be simply proportional to $(2J+1)$. We have checked the effects of this rule on the values of β for the present case with detailed statistical model calculations. Transmission coefficients for the exit channels were calculated with the optical model using the potential parameters of Becchetti and Greenlees[24] and of McFadden and Satchler[25]. These are conveniently summarized by Christensen et al.[9]. Expressions for the level densities $\rho(E)$ and $\rho(E,J)$, which are required to evaluate the relative transition probabilities to continuum states, are also summarized in ref. [9]. Values of the parameters used in the present work are given in table 2.

Table 3 compares the values of β obtained with the $(2J+1)$ rule to those obtained with statistical model calculations. In most cases the two values of β agree within 10%, indicating that the β calculations are nearly model independent. Further details and the results of the cross sections calculations are given in the following subsections.

3.1.1 RESIDUES FROM SINGLE PARTICLE EVAPORATION

The residual nuclei ^{23}Mg, ^{23}Na and ^{20}Ne can be formed by evaporation from the ^{24}Mg compound system of a neutron, proton and α particle, respectively. The relative populations $R_l(J_i)$ of the bound states in the final nuclei were calculated as

$$R_l(J_i) = (2J_i + 1)\ T_l \qquad (2)$$

where J_i is the spin of the i^{th} final state and T_l is the sum over orbital angular momenta of transmission coefficients for particles of appropriate type and energy. Transmission coefficients were calculated with the

statistical model code "HAUSER 4"[26]. The relative populations determined in this way differ from those obtained from the $(2J+1)$ rule alone mainly by the decrease in importance of highly excited states. In eq. (2), it is assumed that the contributions to T_l from increasing orbital angular momenta can be summed until the contributions from higher l-values are negligible, without being limited by the J-values of the ^{24}Mg compound nucleus. Because of the very high compound nucleus excitation, this assumption causes no significant error.

Final states with excitation energies up to 3.8 MeV in ^{23}Mg and 4.8 MeV in ^{23}Na were considered. These limitations are imposed by a lack of knowledge of the spins and branching ratios of higher excited states. Since ^{23}Mg β-decays with a 9% branch to the first excited state of ^{23}Na, with a lifetime short compared to data accumulation times, the ^{23}Na cross sections deduced from the 440 keV γ-ray yield should be decreased by 9% of the ^{23}Mg cross sections. However, since the ^{23}Mg yields are only about 20% of the ^{23}Na + ^{23}Mg yields, the correction is very small. The relatively small probability of single neutron evaporation has been noted before in reactions with small Q-values[22].

States in ^{20}Ne up to 9.12 MeV were considered in the calculations of β for this nucleus. Except for the unnatural parity states at 4.97 and 7.01 MeV, it is possible for states of excitation above 4.73 MeV, to decay by α-emission to the ground state of ^{16}O. For the higher states $R_l(J_i)$ was therefore multiplied by the ratio of transmission coefficients for E1 plus M1 γ-decay to the sum of transmission coefficients for γ-decay and α-decay of appropriate angular momentum. One result of this competition between α- and γ-decay is that states in ^{20}Ne above 7.2 MeV contribute only a few percent to the total ^{20}Ne production cross section.

The results of the cross section calculations are shown in fig. 7 and

Table 4

tabulated in table 4. The overall systematic uncertainty in these results is estimated as ± 15%, resulting from the quadratic combinations of 5% uncertainties in beam current integration, target ^{10}B content, and photopeak detection efficiency, with 10% uncertainties in the β values. The statistical uncertainties in the cross sections at low energies are indicated in fig. 7. At higher energies these uncertainties are roughly ± 15% for ^{23}Mg, ± 4% for ^{23}Na and ± 10% for ^{20}Ne.

3.1.2 TWO-PARTICLE EVAPORATION RESIDUES

The nuclei ^{23}Mg, ^{23}Na and ^{20}Ne may be formed at sufficiently high excitation energy that a second particle can be evaporated. The relative probability for forming the intermediate system was taken as

$$R_1(E_{x1}) = T_1\, \rho(E_{x1})\, \Delta E_{x1} \quad , \tag{3}$$

where $\rho(E_{x1})\, \Delta E_{x1}$ is the number of states with excitation energy between E_{x1} and $E_{x1} + \Delta E_{x1}$. Particle emission from these states can populate bound states of ^{19}F, ^{19}Ne, ^{22}Ne, ^{22}Na, ^{22}Mg and ^{16}O. To calculate relative populations $R_2(J_f)$ of these states, eq. (3) is multiplied by $(2J_f + 1)\, T_2$ where T_2 is the transmission coefficient (summed over orbital angular momenta) for emission of the second particle and J_f is the spin of the final state. The product is summed over particle-unstable excitation energies of the intermediate system with the result:

$$R_2(J_f) = \Sigma_{E_{x1}}\, T_1\, \rho(E_{x1})\, \Delta E_{x1}\, T_2\, (2J_f + 1) \quad . \tag{4}$$

The number of discrete states considered in the evaluation of eq. (4) for each residue is indicated in table 3. For the exit channels $^{19}F + \alpha + p$, $^{19}Ne + \alpha + n$ and $^{22}Na + p + n$, particles 1 and 2 may be emitted in either

order. For these cases, eq. (4) was evaluated for both possibilities and the results were added. The relative population of the ground state of ^{16}O was calculated by evaluating eq. (4) for $E_{x1} > 9.1$ MeV and adding the population from the α decay of lower energy discrete states in ^{20}Ne calculated as previously described.

With the exception of ^{22}Mg, γ-rays characteristic of all of the possible two-particle evaporation residues were observed. Failure to observe the ^{22}Mg + 2n channel is not surprising in view of the relatively small probability for single neutron evaporation and the small number of particle-stable states in ^{22}Mg. In any event, since ^{22}Mg decays quickly to excited states of ^{22}Na, ^{22}Mg production cross sections will be included in those for ^{22}Na production deduced from the yields of 583 keV γ-rays.

Results of cross section calculations for production of two-particle evaporation residues are shown in fig. 8 and tabulated in table 4. Systematic uncertainties in these results are estimated to be ± 18% for ^{22}Na and ± 15% for the others. The higher figure for ^{22}Na reflects an additional 10% uncertainty from ^{12}C target impurities. Statistical uncertainties at low energies are indicated in fig. 8. At higher energies, statistical uncertainties are approximately ± 6% for ^{16}O, and less than ± 3% for the other channels.

3.1.3 TOTAL FUSION CROSS SECTIONS

Although it is energetically possible for additional particles to be evaporated, no radiation characteristic of a three-particle evaporation residue was detected, with the exception of ^{21}Ne. In calculating total fusion cross sections as the sum of cross sections for individual processes, however, three-particle evaporation residues should be included.

The relative probability that the two-particle residues are formed in

particle-unstable states was approximated by

$$R_2(E_{x2}) = \Sigma_{E_{x1}} \Sigma_{E_{x2}} T_1\, \rho(E_{x1})\Delta E_{x1}\, T_2\, \rho(E_{x2})\Delta E_{x2}\langle 2J_f + 1\rangle \quad , \qquad (5)$$

where $\rho(E_{x2})\Delta E_{x2}$ is the number of states in the two-particle evaporation residue with excitation energy between E_{x2} and $E_{x2} + \Delta E_{x2}$. At each center-of-mass energy the summations are over the excitation energies consistent with energy conservation. The average weighting factor $\langle 2J_f + 1\rangle$ was calculated from

$$\langle 2J_f + 1\rangle = \int \rho(E_{x2}, J_f)(2J_f + 1)dJ_f / \int \rho(E_{x2}, J_f)dJ_f \quad , \qquad (6)$$

and had values between 4.5 and 5.5 for all cases considered.

The contributions of three-particle evaporations were included in the cross sections for production of two-particle evaporation residues by dividing the latter by

$$F = \frac{\Sigma_f R_2(J_f)}{R_2(E_{x2}) + \Sigma_f R_2(J_f)} \quad , \qquad (7)$$

where the bound state fraction F represents the probability that when a residue is formed, it is formed in a particle-stable state. Values of F for ^{19}Ne and ^{22}Ne differ from unity by only a few percent at the very highest c.m. energies. Values of F for ^{19}F vary more strongly with energy and are shown in fig. 9.

The calculated bound state fractions for ^{16}O are also shown in fig. 9. These were calculated by explicitly treating as bound states the five unnatural parity states in ^{16}O between 10- and 13-MeV. For the unbound states, eq. (5) was evaluated with the actual number of states in each interval ΔE_{x2} used rather than a parametrized density of states. The small values of the

bound state fraction at higher energies imply that three-particle evaporations contribute significantly to the total fusion cross section.

Bound state fractions for ^{16}O were therefore calculated several different ways. First, several parametrizations for the density of states in ^{20}Ne were used without significantly altering the results shown in fig. 9. Second, parametrized densities of states in ^{16}O above 9-MeV excitation were used in eq. (5) to calculate relative populations of continuum states. It was assumed that only half of these states have natural parity and only half the calculated relative population was used as $R_2(E_{x2})$ in eq. (7). The other half was added to the sum of relative populations of bound states, taken as all states below 9-MeV excitation. Results of the two calculations agree at the lowest energies. As energy increases, the second calculation yields larger values of the bound state fraction. At $E_{c.m.} = 6.0$ MeV the discrepancy is 10%, at 7.5 MeV the discrepancy is 20%.

The case of ^{21}Ne, which may be formed by proton evaporation from ^{22}Na, provides another way of checking calculations of bound state fractions. Yields of 351 keV γ-rays were used to deduce ^{21}Ne production cross sections. Values of β were calculated assuming successive proton and deuteron evaporation from ^{24}Mg. These cross sections are also shown in fig. 8 and table 4. The sum of ^{21}Ne and ^{22}Na production cross sections was compared to ^{22}Na cross sections corrected for additional particle evaporations with eq. (7). The sum is approximately 10% higher over the entire energy range. Unfortunately, the ± 20% uncertainty in ^{21}Ne cross sections at high energies arising from the uncertainty in ^{12}C target impurity content somewhat vitiates the check on the bound state fraction calculation.

Total fusion cross sections were obtained by adding the single-particle evaporation cross sections and the two-particle evaporation cross sections corrected for possible three-particle evaporations. The sum of ^{21}Ne and ^{22}Na cross sections was used rather than the corrected ^{22}Na cross sections.

Fig. 10

The results are given in table 4 and shown in fig. 10. At energies above $E_{c.m.} = 4$ MeV uncertainties arising from counting statistics are generally ± 3%. At lower energies these uncertainties are consistent with the scatter of the points. If the three-particle evaporation processes are neglected for the moment, systematic uncertainties in the total fusion cross sections should be less than the ± 15% uncertainty in the individual reaction cross sections. Three-particle evaporations contribute 20% to the total fusion cross section at the highest energy and only a few percent at the lowest. The contributions to the systematic error from three-particle evaporations are difficult to estimate. A 25% error in the calculation of each bound state fraction will be reflected as a 10% error in the fusion cross section at $E_{c.m.} = 7.5$ MeV. Except for the three lowest energies where the statistical errors are relatively large, as shown in fig. 12, the best estimate of the overall uncertainty in the total fusion cross section ranges from ± 15% at the lowest energies to ± 20% at the highest energies reported here.

3.2 ELASTIC SCATTERING CROSS SECTIONS

As previously noted, the yields Y of ^{14}N ions elastically sacttered from ^{10}B were measured relative to those scattered from gold. The ^{10}B differential scattering cross section is therefore

$$\left(\frac{d\sigma}{d\Omega}\right)_{^{10}B} = \frac{Y(^{10}B)}{Y(Au)} \; R \left(\frac{d\sigma}{d\Omega}\right)_{Au} , \qquad (8)$$

where R is the ratio of the number of gold atoms to the number of ^{10}B atoms in the target. Rutherford scattering cross sections, $(d\sigma/d\Omega)_{Au}$, were used to describe the scattering from gold.

Fig. 11

Figure 11 displays the energy dependence of the ^{10}B scattering cross

sections, presented as the ratio to Rutherford scattering. These results have been normalized to Rutherford scattering at low energies. If the measured ratio R is used in eq. (8), results are higher by 10%. This figure is consistent with the accuracy with which R was determined in the proton and α-particle scattering measurements, and is compatible with an estimated systematic uncertainty of ± 5% in the results shown. Although the deviation of the data points in Fig. 11 from the smooth curves are consistent with the ± 5% statistical accuracy of the data, there is some evidence for weak oscillations around the smooth curves.

4. Conclusions

Figure 10 compares the results of the present measurement of the total fusion cross sections with those of High and Čujec[14]. Near $E_{c.m.} = 3.5$ MeV, our data are approximately 20% higher. This is consistent, however, with the combined estimated uncertainty of 25% for the two measurements. At $E_{c.m.} = 6$ MeV the present results are 40% higher than those of High and Čujec. The increasing discrepancy between the present results and those of ref.[14] may be attributed to our corrections for three-particle evaporations. If we neglect these contributions, our results are consistently higher than those of ref.[14] by 20-25%.

Agreement among cross sections measured by the two different experimental techniques has usually been better than in the present case. It is likely that much of the discrepancy here stems from the corrections for unobserved transitions, including three-particle evaporations. The number of open three-particle evaporation channels is greater for $^{14}N + ^{10}B$ reactions than for the other cases studied by both techniques. High and Čujec make a maximum correction of 10% for all non-radiative transitions, while our

corrections for unobserved three-body evaporations alone range up to 20%. High and Čujec use a $(2J+1)$ relative population of bound final states to calculate their corrections. This is likely to underestimate the correction for the population of the ground states of the evaporation residues since the transmission coefficients for particle evaporation to higher states decrease especially rapidly with excitation energy for those channels with small Q-values, such as the three-particle evaporation channels.

To reduce the strong energy dependence of fusion cross sections below the interaction barrier, it is conventional to display the reaction S-factor defined as

$$S = E_{c.m.}\ \sigma\ \exp(2\pi\eta) \qquad (9)$$

where the Sommerfeld parameter $\eta = 13.32\ (\mathrm{MeV}^{1/2})/E_{c.m.}^{1/2}$ for the present case. The S-factor for the fusion of ^{14}N and ^{10}B, as calculated from the present cross sections, is shown in fig. 12. Because the energy dependence of the cross section is diminished in this type of display, structure in the cross section often becomes more evident. To illustrate this, the S-factor for the $^{12}C + ^{12}C$ reaction is also displayed in fig. 12. Clearly, there is no structure in the $^{14}N + ^{10}B$ fusion cross section of magnitude comparable with that shown by the $^{12}C + ^{12}C$ reaction. This conclusion, which agrees with the observations of High and Čujec[14], is not unexpected because of the high excitation energy in the ^{24}Mg compound system and the nature of the interacting nuclei. Since the ^{24}Mg compound excitation energy for $^{14}N + ^{10}B$ is about 15 MeV higher than for $^{12}C + ^{12}C$, it must be anticipated that the higher level density in the $^{14}N + ^{10}B$ case will lead to more complete averaging over compound nuclear states than is the case in $^{12}C + ^{12}C$. In considering the possible influence of entrance channel effects, it may be significant

that the carbon nucleus is much more tightly bound with respect to free nucleons than ^{14}N or ^{10}B. Thus, it seems reasonable that motion of those nucleons not bound in quasi-alpha-particles, during the relatively slow collision of the heavy ions, could effectively damp any resonance effects arising from alpha-particle sub-structure in the participating nuclei.

The incoming-wave boundary condition model has been used to fit the elastic scattering cross sections. The real ion-ion interaction is taken to be a Woods-Saxon potential with a depth of 50 MeV[4]. Adjustable parameters of the model are the diffuseness, a, of the Woods-Saxon well, and either the radius of the well $R_o = r_o(A_1^{1/3} + A_2^{1/3})$ or the radial position, R_b, of the $\ell = 0$ barrier arising from the addition of the Coulomb and real ion-ion potentials. Satisfactory fits to the elastic scattering data were obtained with $R_b = 8.08$ fm, corresponding to $r_o = 1.24$ fm, and $a = 0.50$ fm. The results of the calculations are superimposed on the scattering data in fig. 11. The two parameters can be changed either independently or together by no more than a few percent without visibly worsening the quality of the fits.

The fusion cross section S-factors calculated with these values of the IWBC parameters are superimposed on the present observations in fig. 12. Again, the quality of the fit is sensitive to variations of a few percent in the parameters. The agreement between the calculated and measured S-factors is excellent, with the calculations about 10% lower than the observations at 7.5 MeV, and 10% higher at the lowest energies. Because the IWBC parameters were determined from the $^{14}N + ^{10}B$ elastic scattering measurements in the upper part of the energy region of the present paper, and because transfer reactions are expected to make a negligible contribution because of their non-optimal Q-values, the IWBC fusion cross section calculations should provide a good fit to the measured cross sections, especially at the higher energies. The divergence in slope between our calculations and the observations above

$E_{c.m.}$ = 6 MeV may be evidence that we have overestimated the corrections for three-particle evaporation.

High and Čujec[14] have reported optical model fits to ten sets of fusion and elastic scattering cross sections for the reactions involving boron nuclei. One set, with a real potential well depth of 50 MeV, provided satisfactory fits to all of their data except their $^{14}N + ^{10}B$ fusion cross sections, for which the calculations were about 20% too high. This particular optical model calculation fits the present data well at 3 MeV and lies between the present data and those of ref. [14] at 6 MeV.

When all of the experimental evidence, and the various fits are considered together, it appears that High and Čujec may have underestimated their non-radiative transition corrections, whereas we may have overestimated the three-particle evaporation corrections. Since statistical model calculations exhibit some features which disagree with experiment, such as their failure to predict correctly the ratio of α-particle and proton emission[9], it appears that a more complete (and vastly more expensive) calculation of two- and three-particle evaporation channels would be unlikely to lead to a more trustworthy prediction of the absolute cross section than is available from the present work and that of reference [14].

References

1) W. A. Fowler, G. R. Caughlan and B. A. Zimmerman, Ann. Rev. Astron. Astrophys. 13 (1975) 69

2) W. A. Fowler and F. Hoyle, Astrophys. J. Suppl. No. 91, 9 (1964) 201

3) R. G. Stokstad, Z. E. Switkowski, R. A. Dayras and R. M. Wieland, Phys. Rev. Lett. 37 (1976) 888

4) P. R. Christensen and Z. E. Switkowski, Nucl. Phys. A280 (1977) 205

5) M. D. High and B. Čujec, Nucl. Phys. A259 (1976) 513

6) M. D. High and B. Čujec, Nucl. Phys. A282 (1977) 181; K.-U. Kettner, H. Lorenz-Wirzba, C. Rolfs and H. Winkler, Phys. Rev. Lett. 38 (1977) 337; M. G. Mazarakis and W. E. Stephens, Phys. Rev. C7 (1973) 1280; J. R. Patterson, H. Winkler and C. S. Zaidins, Astrophys. J. 157 (1969) 367

7) J. R. Patterson, B. N. Nagorcka, G. D. Symons and W. M. Zuk, Nucl. Phys. A165 (1971) 545

8) B. Čujec and C. A. Barnes, Nucl. Phys. A266 (1976) 461

9) P. R. Christensen, Z. E. Switkowski and R. A. Dayras, Nucl. Phys. A280 (1977) 189

10) R. G. Stokstad, Lecture Notes in Physics, Vol. 22 (Springer-Verlag, 1973)

11) D. L. Hanson, R. G. Stokstad, K. A. Erb, C. Olmer, M. W. Sachs, and D. A. Bromley, Phys. Rev. C9 (1974) 1760

12) N. Marquardt, R. Volders, C. Cardinal and J. L'Ecuyer, Phys. Rev. Lett. 33 (1974) 1389

13) Z. E. Switkowski, R. G. Stokstad and R. M. Wieland, Nucl. Phys. A274 (1976) 202

14) M. D. High and B. Čujec, Nucl. Phys. A278 (1977) 149

15) J. C. Overley and W. Whaling, Phys. Rev. 128 (1962) 315; J. C. Overley, Ph.D. thesis, Caltech (1961) unpublished

16) D. S. Andreev, V. D. Vasil'ev, G. M. Gusinskii, K. I. Erokhina and I. Kh. Lemberg, Izvestia Akad. Nauk (USSR), Bull. Fiz. Ser. 25 (1961) 842

17) F. Ajzenberg-Selove and T. Lauritsen, Nucl. Phys. A227 (1974) 1

18) Z. E. Switkowski and R. A. Dayras, Nucl. Instr. and Meth. 128 (1975) 9

19) C. A. Barnes, J. C. Overley, Z. E. Switkowski and T. A. Tombrello, Appl. Phys. Lett. 31 (1977) 239

20) L. C. Northcliffe and R. F. Schilling, Nucl. Data Tables A7 (1970) No. 3

21) S. G. Boydell, Ph.D. thesis, University of Melbourne (1973) unpublished; see also A. Anttila, J. Keinonen, M. Hautala and I. Forsblom, Nucl. Instr. and Meth. 147 (1977) 501 and references therein

22) Z. E. Switkowski, R. G. Stokstad and R. M. Wieland, Nucl. Phys. A279 (1977) 502

23) P. M. Endt and C. Van der Leun, Nucl. Phys. A214 (1973) 1

24) F. D. Becchetti, Jr. and G. W. Greenlees, Phys. Rev. 182 (1969) 1190

25) L. McFadden and G. R. Satchler, Nucl. Phys. 84 (1966) 177

26) F. M. Mann, Hanford Engineering and Development Laboratories Report No. HEDL-TME-7680 (1976) unpublished

Table 1

Fusion γ-Ray Photopeak Identification[a)]

Peak #	E_γ (keV)	Source	Peak #	E_γ (keV)	Source
1	74	$^{22}Na(2 \rightarrow 1) + pn$[c)]	12	671	^{63}Cu Coulomb Exc.
		Pb X-ray	13	718	^{10}B Coulomb Exc.
2	85	Pb X-ray	14[b)]	890	$^{22}Na(3 \rightarrow 0) + pn$[c)]
3[b)]	110	$^{19}F(1 \rightarrow 0) + \alpha p$	15	1233	$^{19}F(3 \rightarrow 1) + \alpha p$
4[b)]	197	$^{19}F(2 \rightarrow 0) + \alpha p$		1236	$^{19}Ne(3 \rightarrow 2) + \alpha n$
5[b)]	238	$^{19}Ne(1 \rightarrow 0) + \alpha n$	16[b)]	1275	$^{22}Ne(1 \rightarrow 0) + pp$
6[b)]	275	$^{19}Ne(2 \rightarrow 0) + \alpha n$	17	1369	$^{22}Na(6 \rightarrow 1) + pn$[c)]
7[b)]	351	$^{21}Ne(1 \rightarrow 0) + ppn$		1369	$^{24}Mg(1 \rightarrow 0)$[f)]
8[b)]	440	$^{23}Na(1 \rightarrow 0) + p$	18	1400	$^{22}Na(7 \rightarrow 1) + pn$[c)]
9[b)]	451	$^{23}Mg(1 \rightarrow 0) + n$	19	1528	$^{22}Na(4 \rightarrow 0) + pn$[c)]
10	511	β^+ annihilation	20	1554	$^{22}Na(8 \rightarrow 2) + pn$[c)]
11[b)]	583	$^{22}Na(1 \rightarrow 0) + pn$[c)]	21	1634	$^{20}Ne(1 \rightarrow 0) + \alpha$
	585	$^{25}Mg(1 \rightarrow 0)$[d)]	—[b,e)]	6131	$^{16}O(2 \rightarrow 0) + \alpha\alpha$

a) See fig. 5.

b) Used in cross section determinations.

c) Also formed through $^{14}N + ^{12}C$ fusion.

d) Formed through $^{14}N + ^{12}C$ and $^{14}N + ^{16}O$ fusion.

e) Observed in a second data set at lower gain.

f) Formed through $^{14}N + ^{12}C$.

Table 2

Level Density Parameters[a)]

Nucleus	T (MeV)	E_0 (MeV)	U' (MeV)	a $(MeV)^{-1}$	Δ
^{16}O	3.09	2.74	11.9	2.40	7.08
^{19}F	2.96	-3.89	10.4	2.15	-0.68
^{19}Ne	3.85	-6.05	10.4	1.70	-3.99
^{20}Ne	2.61	1.65	10.0	2.84	5.02
^{22}Ne	2.70	-2.21	9.3	2.27	-0.02
^{22}Na	2.68	-3.75	9.3	2.66	-1.08
^{23}Na	2.16	-0.54	9.0	3.57	2.67
^{23}Mg	1.92	0.37	9.0	4.25	4.00

a) For definitions of parameters, see ref.[9)].

Table 3

Summing-Branching Corrections

Nucleus	E_γ (keV)	No. of levels[a)]	$\beta_{(2J+1)}$	$\beta_{Statistical}$	
				$E_{c.m.}$ = 2.5 MeV	$E_{c.m.}$ = 7.5 MeV
^{16}O	6131	11[b)]	0.498	0.436	0.474
^{19}F	110	16	.312	.337	.321
	197	16	.517	.486	.505
^{19}Ne	238	8	.521	.530	.529
	275	8	.251	.228	.317
^{20}Ne	1634	8	.867	.874	.874
^{21}Ne	351	10	.674	.473[c)]	.648
^{22}Ne	1275	10	.839	.840	.839
^{22}Na	583	16	.463	.393	.451
	890	16	.158	.186	.163
^{23}Na	440	12	.608	.608	.608
^{23}Mg	451	8	.656	.642	.642

a) Includes states of known decay scheme up to 2 MeV above the first particle emission threshold.

b) Includes 5 unnatural parity states between 10 and 13 MeV.

c) $E_{c.m.}$ = 4 MeV.

Table 4

$^{14}N + {}^{10}B$ Reaction Cross Sections

$E_{c.m.}$ (MeV)	Partial Cross Sections[a] (b)									σ_{fus} (b)
	^{16}O	^{19}F	^{19}Ne	^{20}Ne	^{21}Ne	^{22}Ne	^{22}Na	^{23}Na	^{23}Mg	
2.89	1.76(-6)	1.09(-6)					9.27(-7)	1.79(-7)		4.07(-6)
3.10		2.43						5.90		
3.22	2.43	3.46		5.05(-7)		4.36(-7)	2.43(-6)	1.26(-6)		1.07(-5)
3.31	6.14	4.93		7.83		1.67(-6)	4.18	2.48	9.06(-8)	2.09
3.39	9.78	7.71		7.39		2.95	7.21	2.72	5.52(-7)	3.26
3.47	1.61(-5)	1.14(-5)		1.01(-6)		3.42	1.10(-5)	4.08	6.78	5.21
3.56	2.28	1.37		2.11		6.75	1.83	6.94	8.81	7.47
3.64	3.64	2.10	3.22(-6)	3.00		1.09(-5)	2.80	8.72	1.41(-6)	1.15(-4)
3.72	4.79	3.37	3.99	4.55	4.00(-6)	1.68	3.86	1.41(-5)	2.09	1.72
3.81	7.39	4.96	4.39	9.46	7.15	2.28	6.98	1.79	2.53	2.68
3.89	1.12(-4)	6.81	7.78	1.05(-5)	4.52	3.46	9.38	2.64	6.80	3.81
3.97	1.71	1.04(-4)	1.14(-5)	1.47	9.91	5.23	1.29(-4)	3.76	5.56	5.64
4.06	2.47	1.53	1.86	1.76	1.34(-5)	7.14	2.00	4.94	1.19(-5)	8.25
4.14	3.57	2.15	2.38	2.70	2.33	1.03(-4)	2.70	6.96	1.22	1.17(-3)
4.23	4.67	3.02	3.79	4.39	3.17	1.39	3.85	9.40	1.57	1.61
4.31	5.86	4.18	5.19	5.30	5.41	1.99	5.42	1.36(-4)	2.76	2.19
4.39	8.00	5.75	6.63	7.37	5.85	2.90	7.11	1.77	3.02	2.96
4.48	1.12(-3)	7.60	1.02(-4)	8.23	9.32	3.61	9.75	2.28	4.28	4.03

Table 4 (continued)

$E_{c.m.}$ (MeV)	Partial Cross Sections[a] (b)									σ_{fus} (b)
	^{16}O	^{19}F	^{19}Ne	^{20}Ne	^{21}Ne	^{22}Ne	^{22}Na	^{23}Na	^{23}Mg	
4.56	1.44	1.03(-3)	1.41	1.32(-4)	1.25(-4)	4.80	1.29(-3)	3.03	5.82	5.34
4.64	1.94	1.34	1.80	1.60	1.55	6.03	1.69	3.83	7.99	7.03
4.73	2.34	1.72	2.19	2.10	2.32	8.01	2.23	4.91	8.89	8.98
4.81	2.85	2.23	2.97	2.40	3.01	9.97	2.82	6.13	1.12(-4)	1.13(-2)
4.89	3.89	2.80	3.75	2.97	3.91	1.27(-3)	3.59	7.54	1.65	1.47
4.98	4.78	3.60	5.04	3.87	5.42	1.63	4.36	9.56	1.93	1.85
5.06	5.52	4.31	6.18	4.55	6.60	1.97	5.48	1.11(-3)	2.34	2.24
5.14	6.95	5.20	7.46	5.65	8.41	2.39	6.75	1.33	2.94	2.75
5.23	7.32	6.35	9.24	6.89	9.98	2.90	8.20	1.61	3.67	3.21
5.31	9.84	7.66	1.12(-3)	7.99	1.30(-3)	3.41	9.73	1.89	4.11	4.00
5.39	1.14(-2)	9.12	1.33	9.03	1.60	4.02	1.16(-2)	2.17	4.55	4.72
5.48	1.34	1.08(-2)	1.60	1.13(-3)	1.94	4.43	1.35	2.49	5.40	5.54
5.56	1.59	1.26	1.95	1.26	2.40	5.51	1.58	2.85	6.75	6.59
5.65	1.86	1.46	2.29	1.44	2.82	6.43	1.81	3.14	8.02	7.68
5.73	2.10	1.68	2.66	1.65	3.36	7.41	2.06	3.59	8.57	8.80
5.81	2.39	1.97	3.23	1.80	4.19	8.28	2.33	4.15	1.05(-3)	1.02(-1)
5.90	2.64	2.22	3.69	2.15	5.04	9.23	2.64	4.68	1.09	1.15
5.98	2.90	2.49	4.08	2.44	5.86	1.06(-2)	2.95	5.06	1.25	1.28
6.06	3.22	2.77	4.60	2.42	6.92	1.21	3.29	5.40	1.37	1.44

Table 4 (continued)

$E_{c.m.}$ (MeV)	Partial Cross Sections[a] (b)									σ_{fus} (b)
	^{16}O	^{19}F	^{19}Ne	^{20}Ne	^{21}Ne	^{22}Ne	^{22}Na	^{23}Na	^{23}Mg	
6.15	3.56	3.06	5.04	2.79	8.01	1.30	3.55	5.96	1.46	1.59
6.23	3.75	3.35	5.73	2.87	9.29	1.40	3.78	6.41	1.75	1.72
6.31	4.31	3.69	6.36	3.35	1.06(-2)	1.54	4.40	6.77	1.71	1.95
6.40	4.35	4.03	7.06	3.75	1.19	1.72	4.58	7.14	1.88	2.07
6.48	5.14	4.27	7.64	3.82	1.33	1.79	5.04	7.78	2.16	2.31
6.56	5.20	4.61	8.38	3.84	1.47	1.93	5.63	8.49	2.40	2.48
6.65	5.80	4.93	9.04	4.27	1.74	2.08	6.10	8.60	2.28	2.73
6.73	6.09	5.26	9.41	3.64	1.93	2.17	6.63	8.85	2.67	2.91
6.81	6.19	5.60	1.06(-2)	4.30	2.08	2.30	7.01	9.03	2.40	3.07
6.90	6.81	5.92	1.04	5.45	2.24	2.43	7.47	9.94	2.60	3.32
6.98	6.89	6.20	1.17	5.28	2.45	2.53	7.79	1.00(-2)	2.75	3.47
7.06	7.57	6.48	1.24	5.16	2.62	2.62	8.51	1.04	2.65	3.74
7.15	7.75	6.77	1.27	5.56	2.73	2.70	8.49	1.09	3.03	3.87
7.23	8.09	7.12	1.38	6.04	2.99	2.78	9.22	1.12	2.73	4.11
7.32	8.48	7.42	1.43	6.56	3.29	2.93	9.46	1.21	2.92	4.33
7.40	8.69	7.67	1.44	6.28	3.53	2.93	9.84	1.16	2.75	4.49
7.48	9.10	7.93	1.62	7.01	3.62	3.14	1.02(-1)	1.21	3.12	4.72

a) Labeled by residual heavy nucleus. Cross sections are obtained by multiplying by 10^x where x is given in parentheses.

Figure Captions

Fig. 1. Partial Q-value scheme for the open reaction channels initiated by $^{14}N + ^{10}B$ fusion. The cross-hatched area represents the region of excitation in ^{24}Mg populated in the present work. All one-, two- and three-particle evaporation channels which are allowed by the reaction Q-values are shown. The dominant γ-ray transitions observed in the deexcitation of evaporation residues are indicated by arrows.

Fig. 2. Pulse-height spectrum of protons scattered from a copper-backed ^{10}B target. The expected positions of the elastic scattering features arising from the various target constituents are indicated by arrows. The region of the ^{10}B scattering peak is shown on an expanded scale in the inset. The beam current and integrated charge for these data were $\sim$ 60 nA and 60 μC, respectively.

Fig. 3. Photopeak yields of 718 keV γ-rays resulting from ^{14}N and ^{16}O ion bombardment of a copper-backed ^{10}B target. The yields have been normalized to calculated Coulomb excitation cross sections which are shown by the solid curves. The error bars on the data points derive from counting statistics alone.

Fig. 4. Relative hydrogen concentration profiles in a copper-backed ^{10}B target. The yields of γ rays depositing more than 3.5 MeV of energy in the NaI(Tl) detector are plotted vs ^{19}F beam energy. The energy-loss target thicknesses are indicated. The 16.44 MeV resonance natural width is 86 keV, which is 40 keV wider than the 6.40 MeV resonance. This accounts for the apparently greater target thickness measured by the higher energy resonance, in spite

of the slightly larger dE/dx for fluorine ions at the lower resonance.

Fig. 5. Gamma-ray pulse height spectrum from $^{14}N + ^{10}B$ reactions. The abscissa for the upper spectrum is at the top of the figure. Numbered full-energy peaks are identified in table 1.

Fig. 6. Pulse-height spectrum of scattered particles detected when a ^{14}N beam is incident on a carbon-film-backed ^{10}B target. Peaks due to ^{14}N ions are labelled by the scattering nuclei. Recoils of target constituents are also indicated.

Fig. 7. Cross sections for production of single-particle evaporation residues from $^{14}N + ^{10}B$ fusion. The error bars ar low energies represent counting statistics alone.

Fig. 8. Cross sections for production of two-particle evaporation residues from $^{14}N + ^{10}B$ fusion. For clarity, data for ^{16}O, ^{19}F and ^{21}Ne have been displaced vertically by the factors indicated. The error bars at low energies derive from counting statistics alone.

Fig. 9. Calculated bound state fractions, F, for ^{16}O and ^{19}F. The bound state fractions for ^{19}Ne, ^{22}Ne and ^{22}Na differ from unity by at most a few percent and are not shown.

Fig. 10. $^{14}N + ^{10}B$ fusion cross sections. The open circles represent the present work; the filled circles are the results of High and Čujec[14].

Fig. 11. $^{14}N + ^{10}B$ elastic scattering differential cross sections presented as the ratio to Rutherford scattering cross sections. The data

have been normalized to Rutherford scattering at low energies. The ordinate for the $\theta_{c.m.} = 74.4^{o}$ scattering is at the right. The solid curves are results of IWBC calculations with $a = 0.50$ fm and $R_b = 8.08$ fm; ($r_0 = 1.24$ fm).

Fig. 12. S-factor for the $^{14}N + ^{10}B$ fusion reaction. The filled circles are from the present work. The error bars at low energies derive from counting statistics alone. The solid curve is the result of an IWBC calculation with a = 0.50 fm and $R_b = 8.08$ fm, as in Fig. 11. For comparison purposes, the $^{12}C + ^{12}C$ fusion S-factors of Patterson et al.[6] are shown as open circles, displaced upwards by a factor of 10 for display clarity.

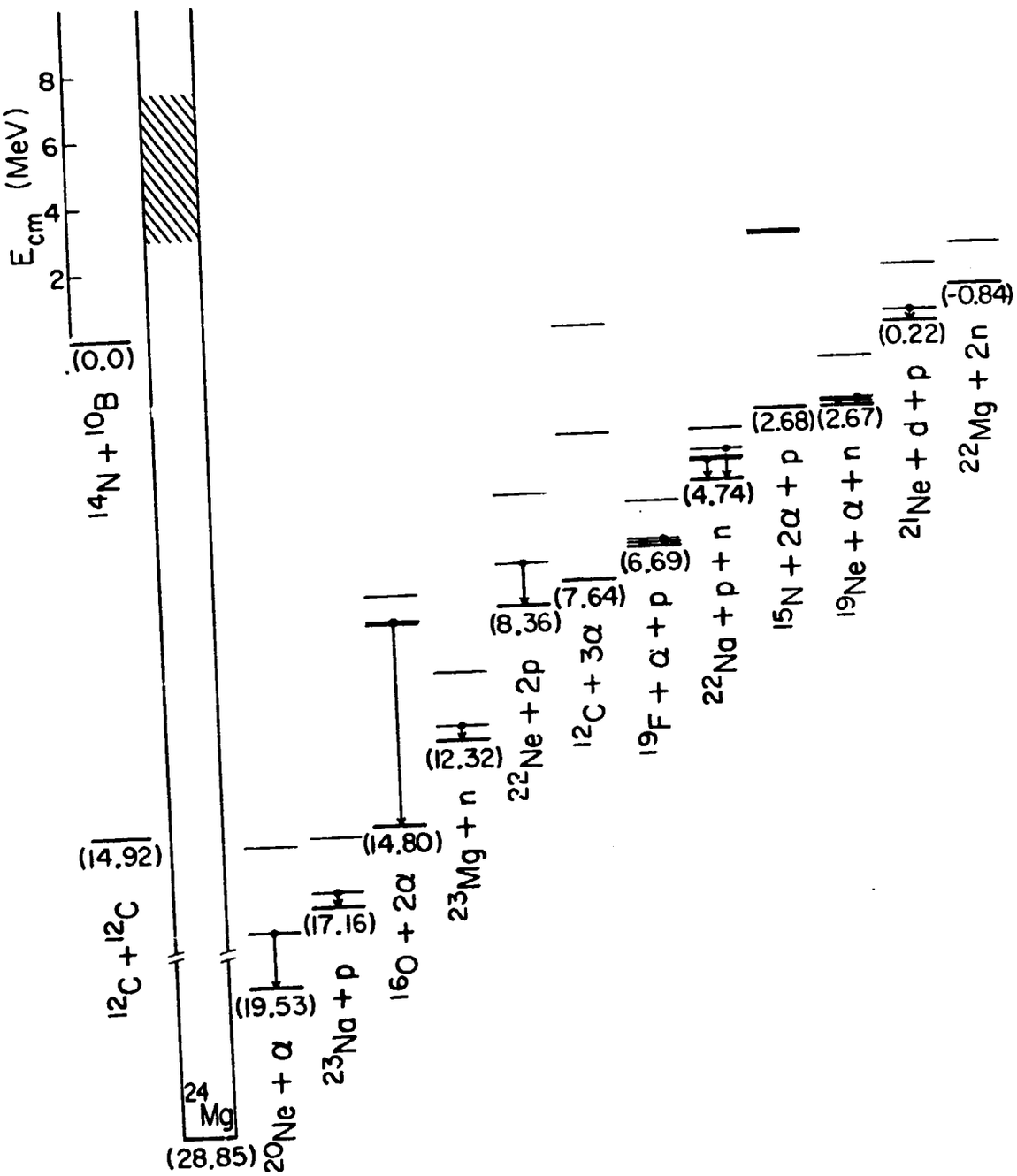
E_{cm} (MeV)
8
6
4
2
(0.0)
$^{14}N + ^{10}B$
(14.92)
$^{12}C + ^{12}C$
(17.16)
$^{23}Na + p$
(19.53)
$^{20}Ne + \alpha$
^{24}Mg
(28.85)
(14.80)
$^{16}O + 2\alpha$
(12.32)
$^{23}Mg + n$
(8.36)
$^{22}Ne + 2p$
(7.64)
$^{12}C + 3\alpha$
(6.69)
$^{19}F + \alpha + p$
(4.74)
$^{22}Na + p + n$
(2.68)
$^{15}N + 2\alpha + p$
(2.67)
$^{19}Ne + \alpha + n$
(0.22)
$^{21}Ne + d + p$
(-0.84)
$^{22}Mg + 2n$

Fig. 1

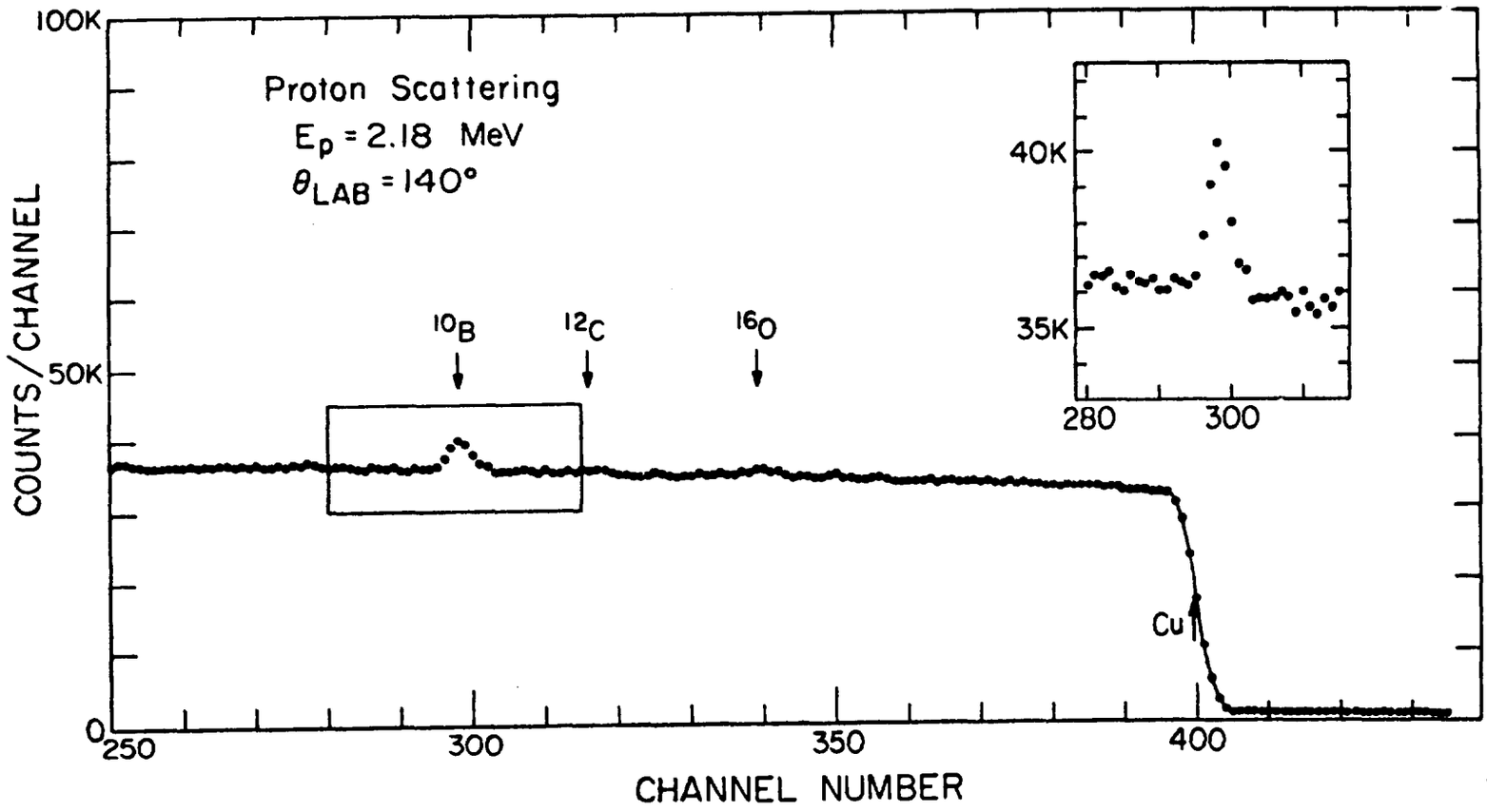
100K
50K
0
COUNTS/CHANNEL
Proton Scattering
E_p = 2.18 MeV
θ_{LAB} = 140°
^{10}B
^{12}C
^{16}O
Cu
40K
35K
280
300
250
300
350
400
CHANNEL NUMBER

FIG. 2

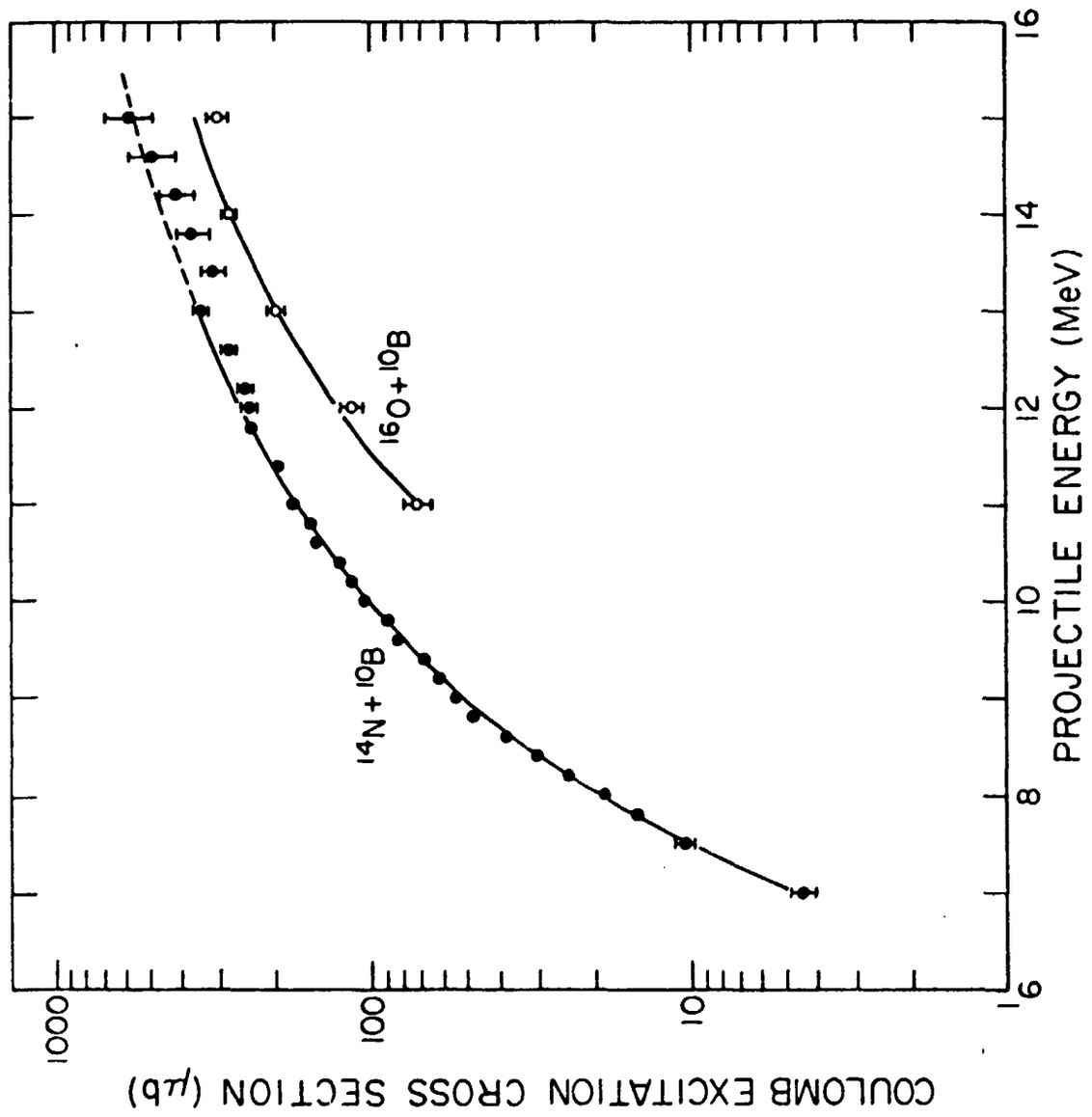
COULOMB EXCITATION CROSS SECTION (μb)
1000
100
10
1
PROJECTILE ENERGY (MeV)
6
8
10
12
14
16
$^{16}O + ^{10}B$
$^{14}N + ^{10}B$

Fig. 3

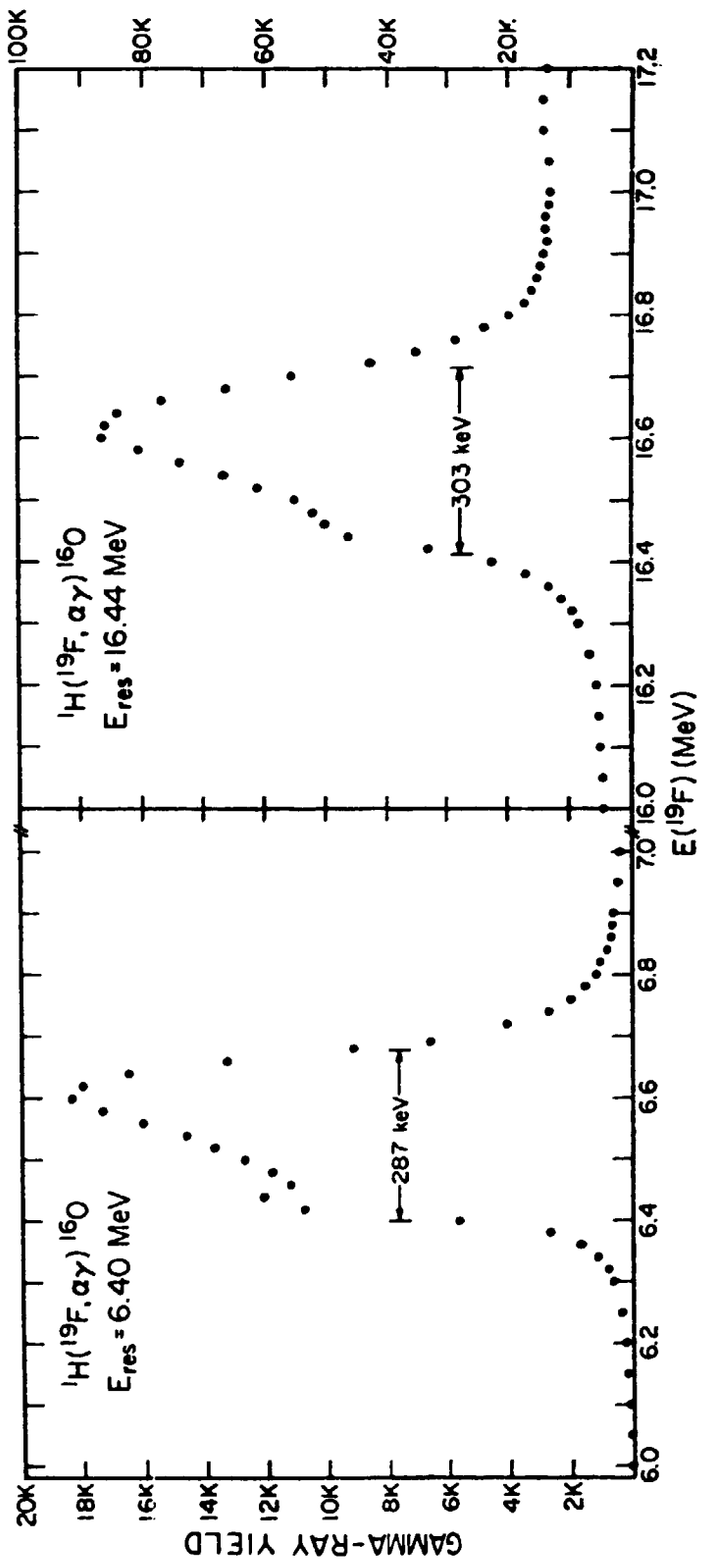
GAMMA-RAY YIELD
E(19F) (MeV)
1H(19F, αγ)16O
Eres = 6.40 MeV
287 keV
1H(19F, αγ)16O
Eres = 16.44 MeV
303 keV

Fig. 4

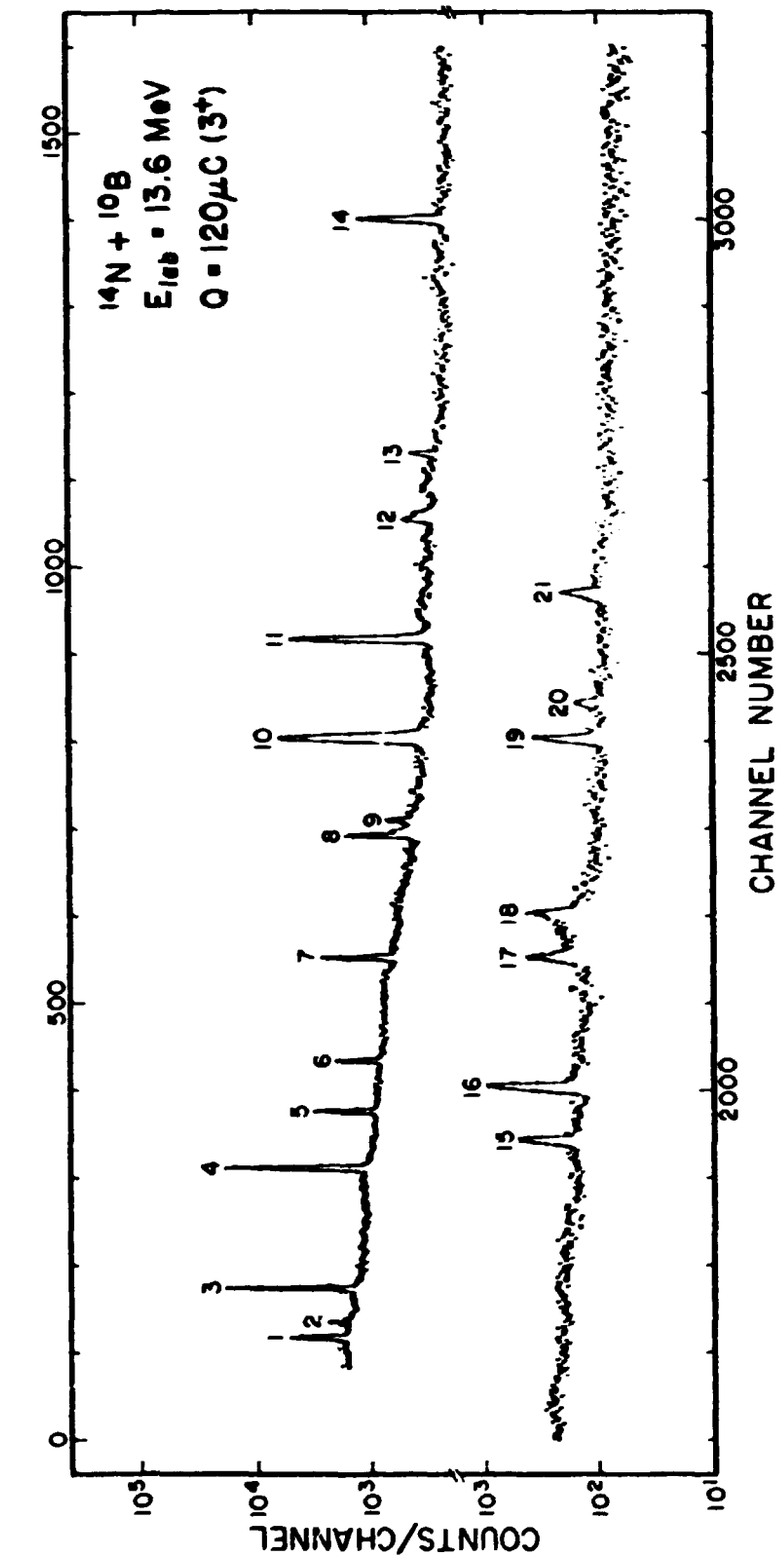
$^{14}N + ^{10}B$
E_{lab} = 13.6 MeV
Q = 120μC (3⁺)
COUNTS/CHANNEL
CHANNEL NUMBER
0
500
1000
1500
2000
2500
3000
10^5
10^4
10^3
10^3
10^2
10^1
1
2
3
4
5
6
7
8
9
10
11
12
13
14
15
16
17
18
19
20
21

Fig. 5

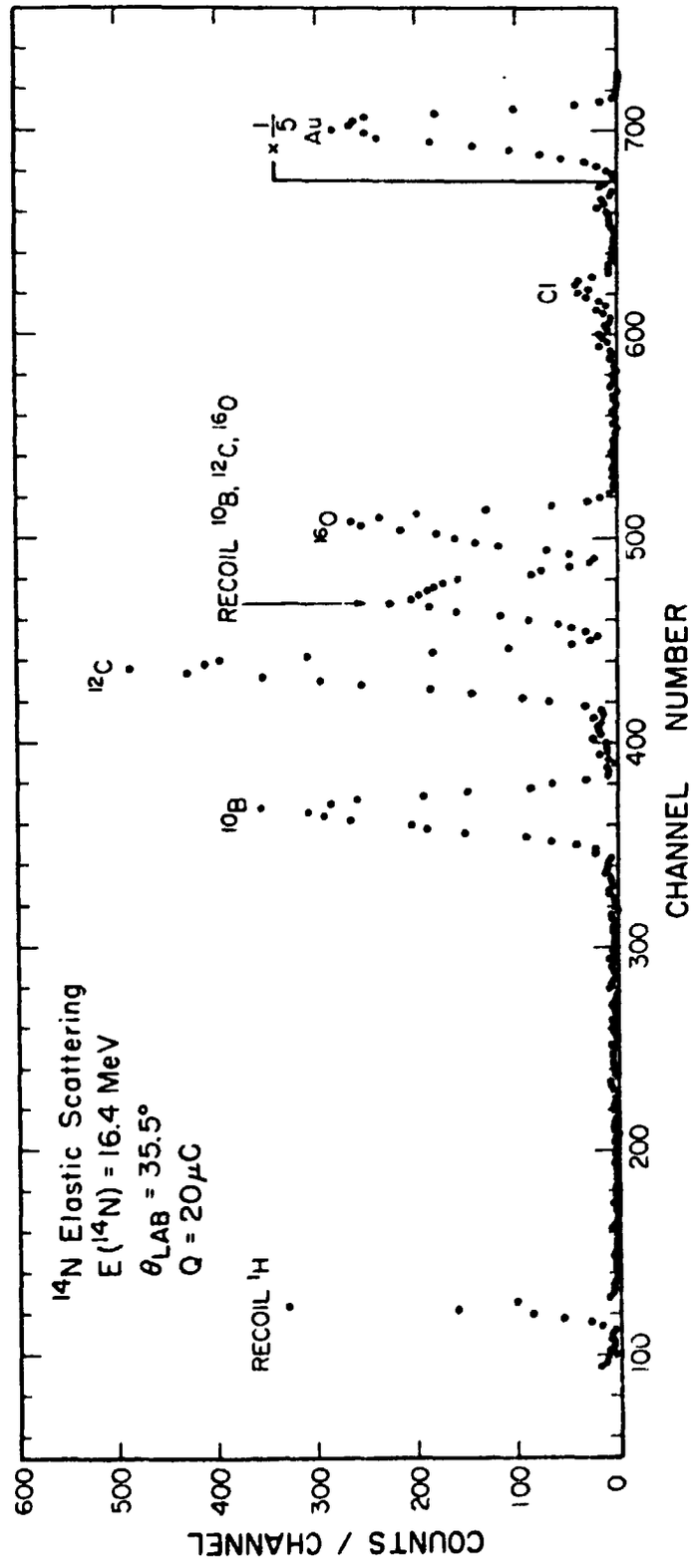
^{14}N Elastic Scattering
E(^{14}N) = 16.4 MeV
θ_{LAB} = 35.5°
Q = 20μC
RECOIL ^{1}H
^{10}B
^{12}C
RECOIL ^{10}B, ^{12}C, ^{16}O
^{16}O
Cl
× 1/5
Au
COUNTS / CHANNEL
CHANNEL NUMBER
0
100
200
300
400
500
600
700

Fig. 6

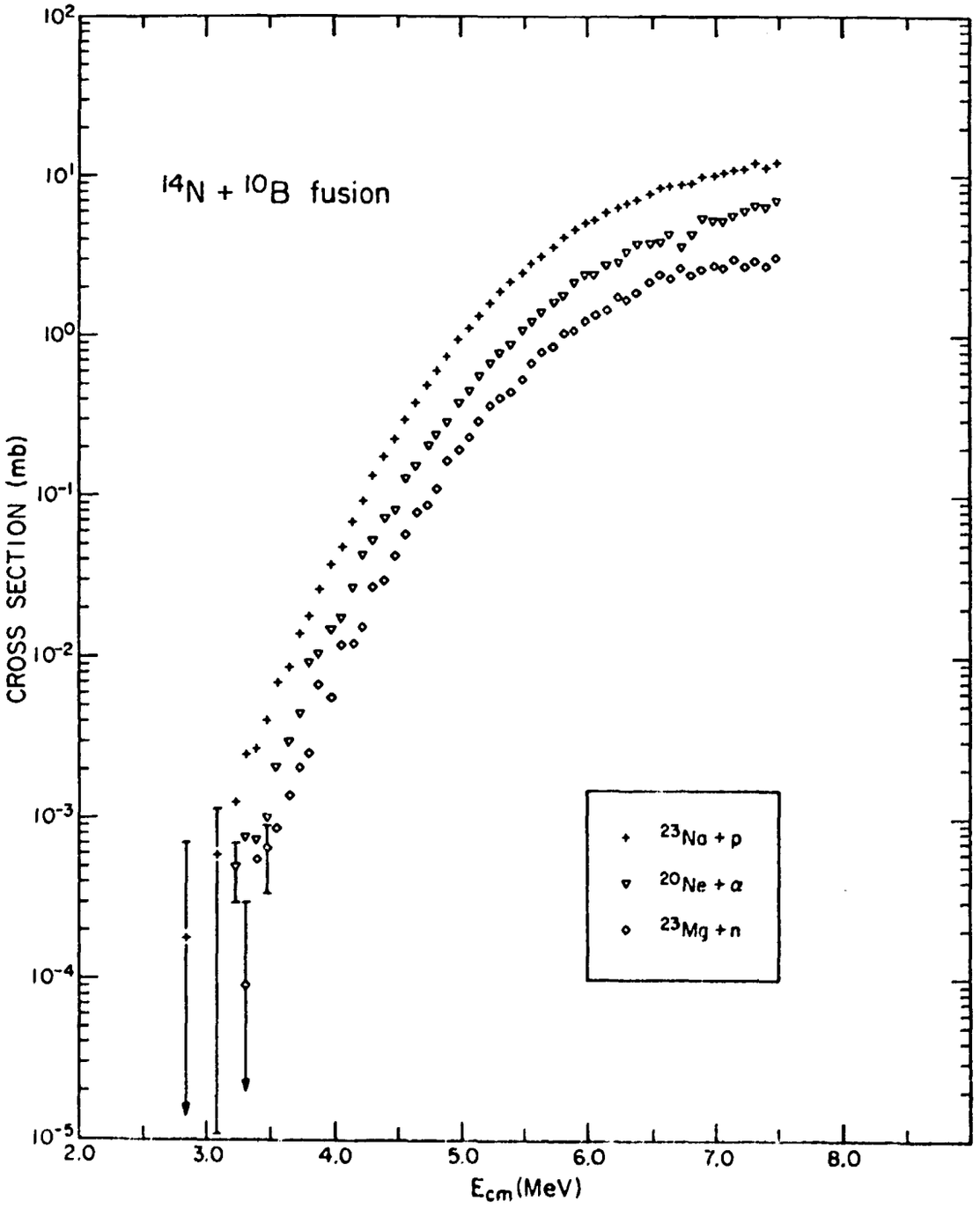
$^{14}N + {}^{10}B$ fusion
CROSS SECTION (mb)
10^{2}
10^{1}
10^{0}
10^{-1}
10^{-2}
10^{-3}
10^{-4}
10^{-5}
2.0
3.0
4.0
5.0
6.0
7.0
8.0
E_{cm}(MeV)
$^{23}Na + p$
$^{20}Ne + \alpha$
$^{23}Mg + n$

Fig. 7

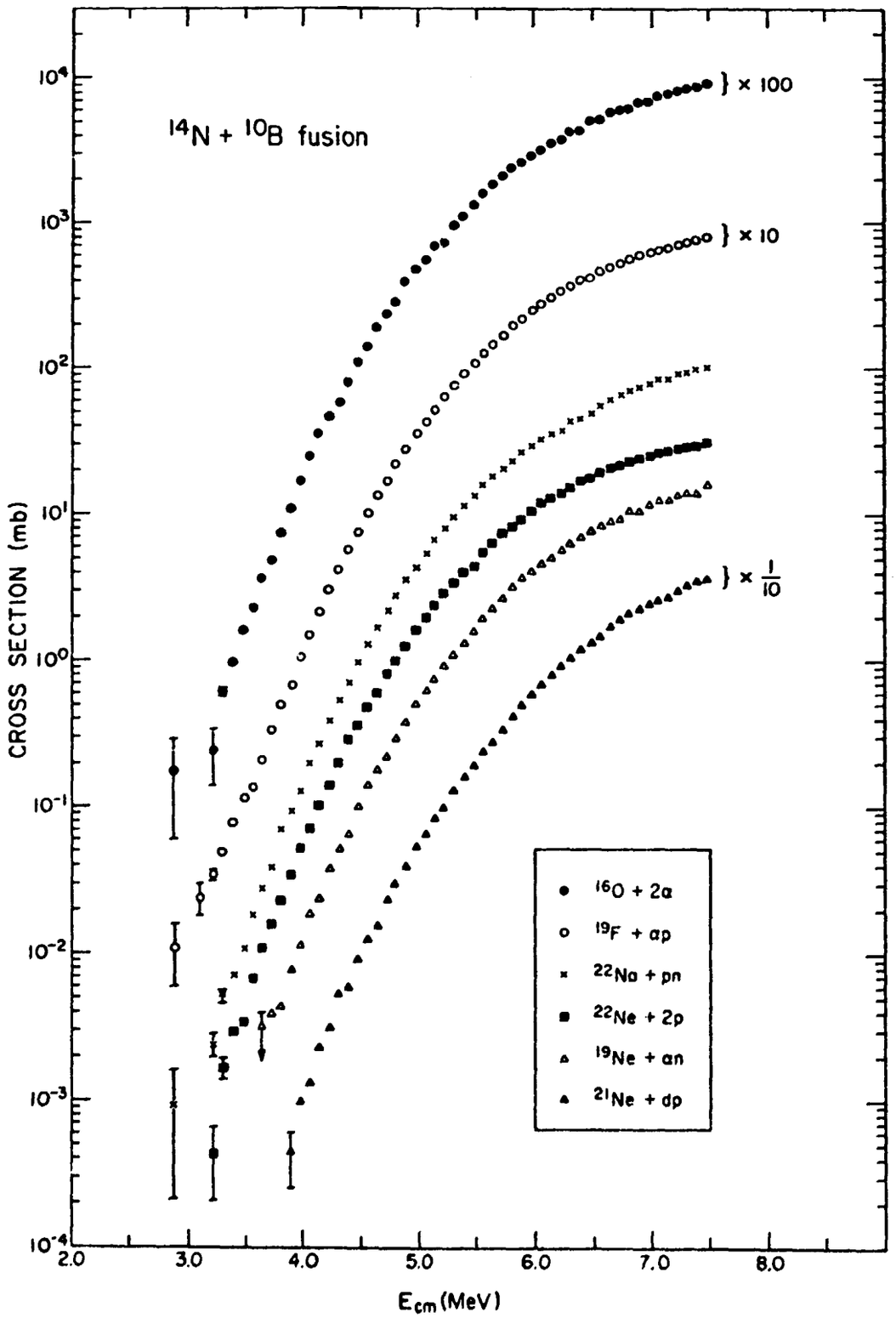
$^{14}N + {}^{10}B$ fusion
} × 100
} × 10
} × 1/10
CROSS SECTION (mb)
E_{cm} (MeV)
$^{16}O + 2\alpha$
$^{19}F + \alpha p$
$^{22}Na + pn$
$^{22}Ne + 2p$
$^{19}Ne + \alpha n$
$^{21}Ne + dp$

Fig. 8

FIG. 9

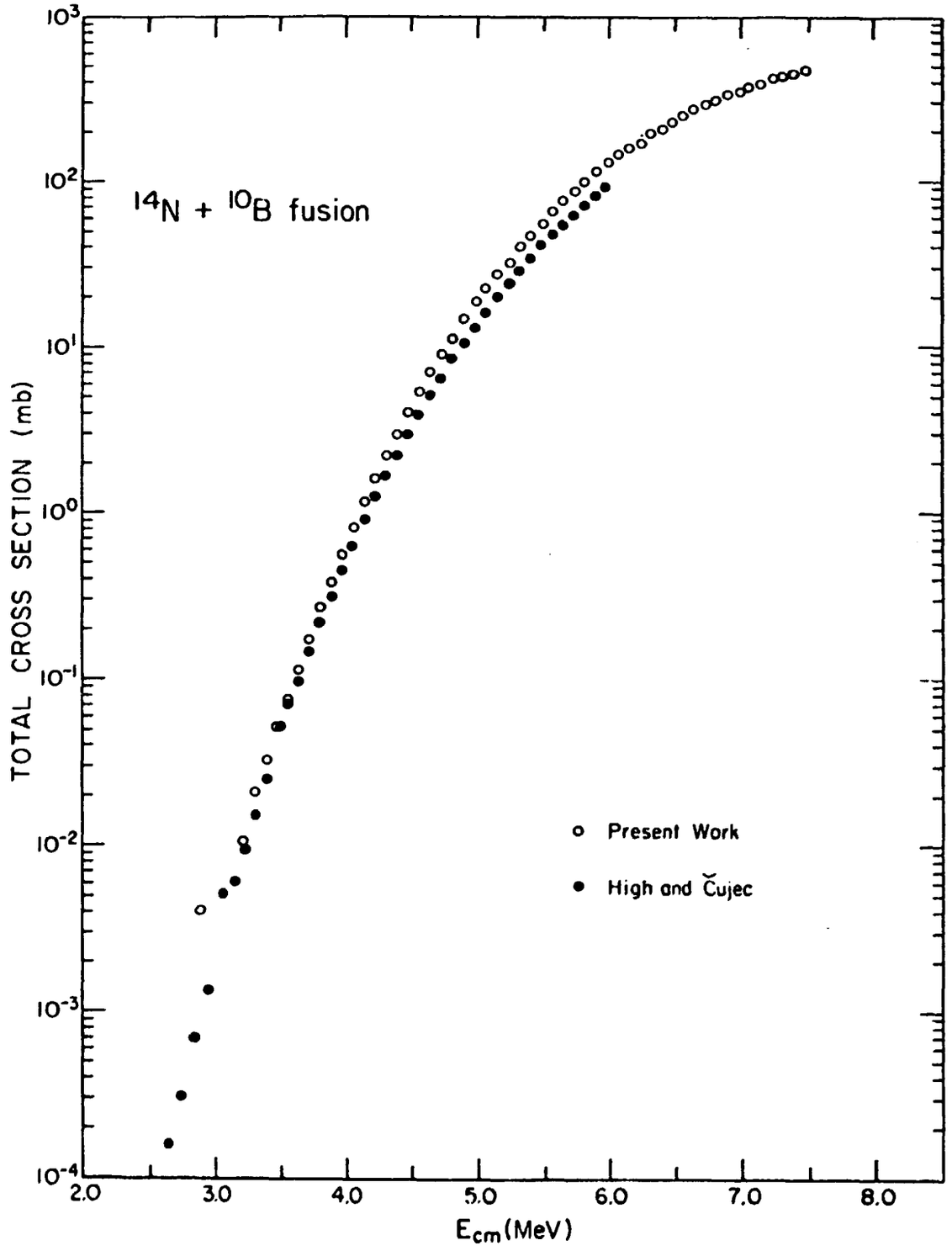
$^{14}N + {}^{10}B$ fusion
TOTAL CROSS SECTION (mb)
E_{cm}(MeV)
Present Work
High and Čujec
10^3
10^2
10^1
10^0
10^{-1}
10^{-2}
10^{-3}
10^{-4}
2.0
3.0
4.0
5.0
6.0
7.0
8.0

Fig. 10

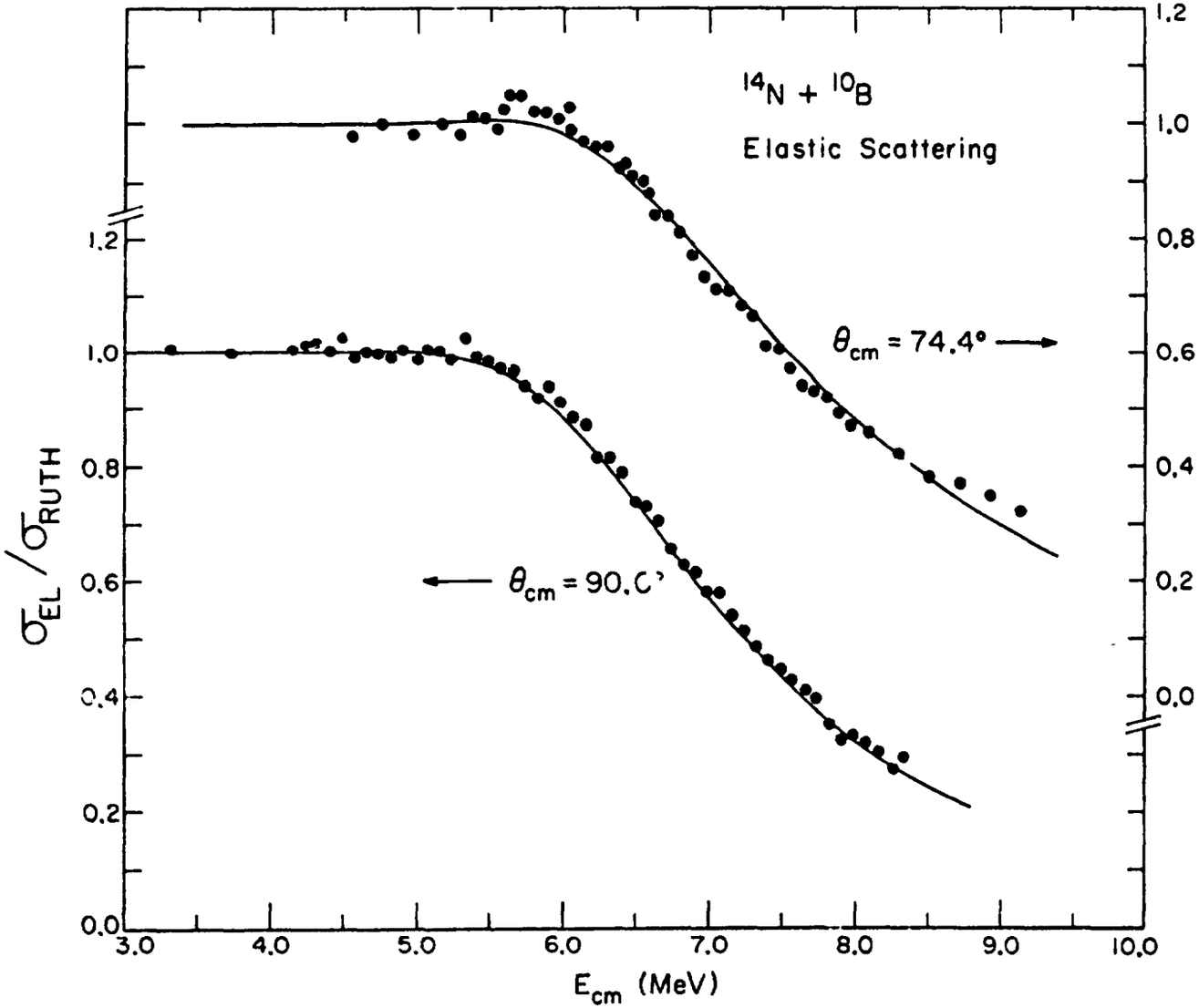
$^{14}N + ^{10}B$
Elastic Scattering
$\theta_{cm} = 74.4°$
$\theta_{cm} = 90.0°$
$\sigma_{EL} / \sigma_{RUTH}$
E_{cm} (MeV)
0.0
0.2
0.4
0.6
0.8
1.0
1.2
3.0
4.0
5.0
6.0
7.0
8.0
9.0
10.0

FIG. 11

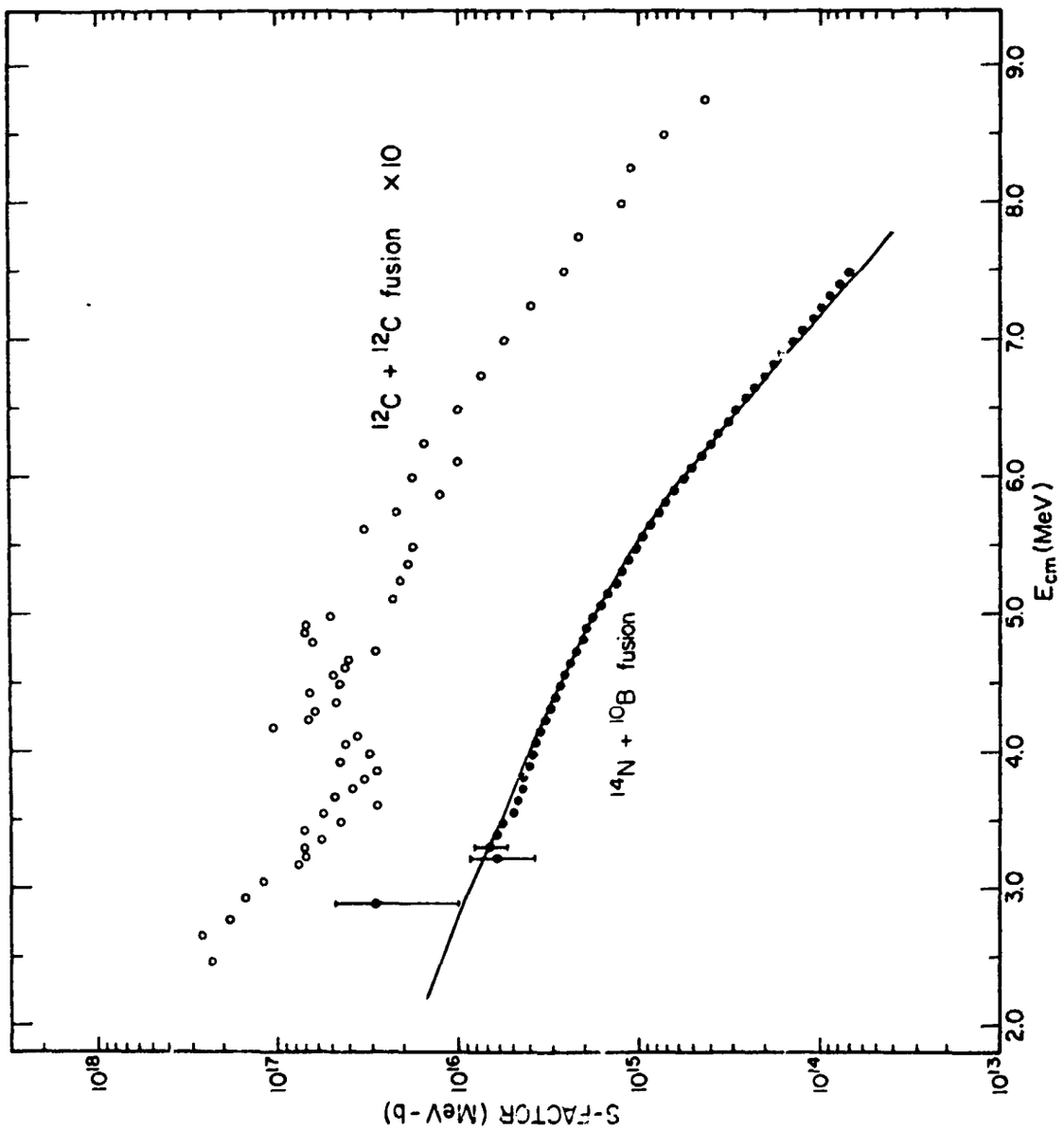
$^{12}C + ^{12}C$ fusion ×10
$^{14}N + ^{10}B$ fusion
S-FACTOR (MeV-b)
E_{cm}(MeV)
10^{18}
10^{17}
10^{16}
10^{15}
10^{14}
10^{13}
2.0
3.0
4.0
5.0
6.0
7.0
8.0
9.0

Fig. 12